

**Title:** Deep Learning for Segmentation-based Hepatic Steatosis Detection on Open Data: A Multicenter International Validation Study

**Authors:** Zhongyi Zhang<sup>1</sup>, Guixia Li<sup>2</sup>, Ziqiang Wang<sup>3</sup>, Feng Xia<sup>4</sup>, Ning Zhao<sup>5</sup>, Huibin Nie<sup>6</sup>, Zezhong Ye<sup>7,8</sup>, Joshua Lin<sup>9</sup>, Yiyi Hui<sup>10\*</sup> & Xiangchun Liu<sup>1\*</sup>

**Affiliations:**

1. Department of Nephrology, The Second Hospital of Shandong University, Shandong University, Jinan, 250033, Shandong, China
2. Department of Nephrology, Shenzhen Third People's Hospital, the Second Affiliated Hospital of Southern University of Science and Technology, Shenzhen, 518112, Guangdong, China
3. Department of Nephrology, The First Affiliated Hospital of Hainan Medical University, Haikou, 570102, Hainan, China
4. Department of Cardiovascular Surgery, Wuhan Asia General Hospital, Wuhan, 430000, Hubei, China
5. The First Clinical Medical School, Shanxi Medical University, Shanxi, 030001, Taiyuan, China
6. Department of Nephrology, Chengdu First People's Hospital, Chengdu, 610095, Sichuan, China
7. Artificial Intelligence in Medicine (AIM) Program, Mass General Brigham, Harvard Medical School, Boston, 02115, MA, USA
8. Department of Radiation Oncology, Dana-Farber Cancer Institute and Brigham and Women's Hospital, Harvard Medical School, Boston, 02115, MA, USA
9. Keck School of Medicine, University of Southern California, Los Angeles, 90033, CA, USA
10. Department of Medical Imaging, Shandong Provincial Hospital Affiliated to Shandong First Medical University, Jinan, 250021, Shandong, China

\* Corresponding authors with the same contribution

Xiangchun Liu, MD, PhD.

Department of Nephrology, The Second Hospital of Shandong University, Shandong University, Jinan, 250033, Shandong, China

Email: [liuxiangchun@sdu.edu.cn](mailto:liuxiangchun@sdu.edu.cn)

Yiyi Hui, MD.

Department of Medical Imaging, Shandong Provincial Hospital Affiliated to Shandong First Medical University, Jinan, 250021, Shandong, China

Email: [huiyiyi@sdfmu.edu.cn](mailto:huiyiyi@sdfmu.edu.cn)

## Abstract

Despite high global prevalence of hepatic steatosis, no automated diagnostics demonstrated generalizability in detecting steatosis on multiple heterogeneous populations. In this retrospective study, we externally validated a fully automated artificial intelligence (AI) system to detect hepatic steatosis. 1,014 non-contrast enhanced chest computed tomography (CT) scans were collected from eight distinct datasets: LIDC-IDRI, NSCLC-Lung1, RIDER, VESSEL12, RICORD-1A, RICORD-1B, COVID-19-Italy, and COVID-19-China. This three-step AI workflow consists of the following: (i) 3D liver segmentation - a 3D U-Net deep learning model developed for liver segmentation and applied externally without retraining. (ii) liver attenuation measurements by three automatic methods: AI on regions of interest (AI-ROI), AI-3D, and AI-2D; (iii) hepatic steatosis detection. The deep-learning segmentation achieved the dice coefficient of  $0.957 \pm 0.046$  (mean  $\pm$  standard deviation). AI-ROI attenuation measurements showed no significant differences compared to expert measurements ( $P > 0.05$ ), but AI-3D and AI-2D were significantly different from the expert ( $P < 0.001$ ). The area under the curve (AUC) of steatosis classification for AI-ROI, AI-3D, and AI-2D are 0.921 (95% CI: 0.883 - 0.959), 0.939 (95% CI: 0.903 - 0.973), and 0.894 (95% CI: 0.850 - 0.938) respectively. If adopted for universal detection, this deep learning system could potentially allow early non-invasive, non-pharmacological preventative interventions for hepatic steatosis. 1,014 expert-annotated liver segmentations of CT images can be downloaded here: [https://drive.google.com/drive/folders/1-g\\_zJeAaZXYXGqL1OeF6pUjr6KB0iqJX](https://drive.google.com/drive/folders/1-g_zJeAaZXYXGqL1OeF6pUjr6KB0iqJX).

**Abbreviations:** 2D = Two-dimensional, 3D = Three-dimensional, AI = Artificial intelligence, AUC = Area under the curve, COVID-19 = Coronavirus Disease 2019, CI = Confidence interval, DSC = Dice coefficient, HU = Hounsfield unit, NIfTI = Neuroimaging Informatics Technology Initiative, NLST = National Lung Screening Trial, ROI = Region of interest, std = Standard deviation.

## Introduction

Hepatic steatosis, also called fatty liver disease, occurs when intrahepatic fat is  $\geq 5\%$  of liver weight<sup>1</sup>. Associated with diabetes, hypertension, obesity, and severe COVID-19 pneumonia<sup>2</sup>, patients with hepatic steatosis experience increased risk for cirrhosis, end-stage liver failure, and early mortality<sup>3</sup>. Non-alcoholic fatty liver disease (NAFLD), a subtype of hepatic steatosis, is recognized as the most common cause of chronic liver disease in the West<sup>4</sup>. Early detection of steatosis might mitigate fat-related liver dysfunction, preventing disease progression that ultimately leads to end-stage liver failures.

Liver biopsy, an invasive procedure, remains the clinical diagnostic standard for hepatic steatosis but carries morbidity risks<sup>5</sup>. Given the constraint of invasive studies, non-invasive imaging methods seem the next-best diagnostics that may ensure reliable, early detection of hepatic steatosis while minimizing morbidity to patients. Non-contrast enhanced computed tomography (CT) has been proven to detect hepatic steatosis reliability in a non-invasive manner<sup>6,7</sup>. A liver attenuation of  $\leq 40$  HU in a clinician-selected region of interest (ROI) would generally indicate moderate-to-severe hepatic steatosis<sup>8,9</sup>. However, this detection method relies on clinicians manually selecting ROIs. The labor-intensive ROI selections prevent population-scale studies, while hepatic steatosis remains unexplored yet in millions of chest CT images scanned for lung cancer<sup>10,11</sup> and COVID-19<sup>12,13</sup>. This bottleneck calls for an automated process.

Deep learning, a form of artificial intelligence (AI), is the frontier of automated medical image analysis<sup>14</sup>. It can automatically segment CT images and detect dysfunctions within seconds<sup>15,16</sup>. However, the current state of deep learning lacks proven generalizability: some methods were developed to segment livers or detect hepatic steatosis<sup>17–20</sup> on plain chest CTs, but none of them were validated externally. Most importantly, none of these studies<sup>17–20</sup> released curated datasets, which could have served as development or validation data to promote deep learning algorithms and hepatic research.

In this retrospective study, we aimed to validate an automated detection system<sup>20</sup> for hepatic steatosis on a population scale: the deep learning model would be compared to the expert on international multicenter multiparameter CT images. The external validation aimed to prove its generalizability across CT imaging protocols and clinical centers, as well as participants' regions, nations, and races in clinical settings worldwide to help detect hepatic steatosis and monitor fat-related dysfunctions.

## Materials and Methods

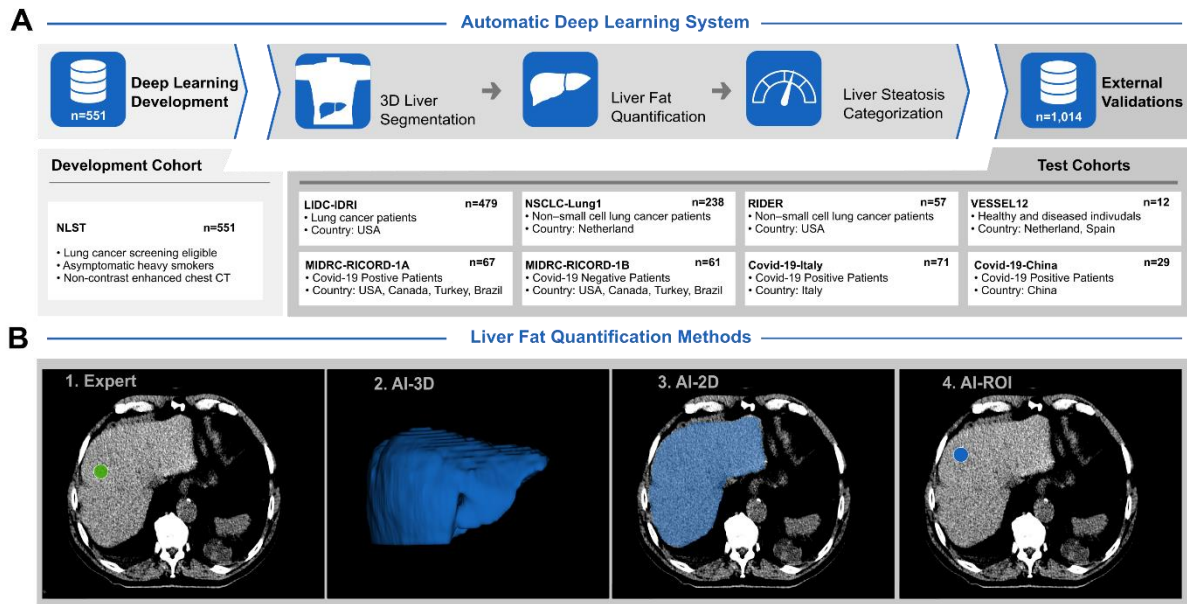


**Figure 1. A:** The deep learning system was developed on NLST and validated on eight distinct datasets for liver segmentation, liver fat quantification, and steatosis classification. **B:** Liver attenuation was measured by experts and artificial intelligence (AI) separately in Hounsfield unit (HU). 1. Expert: Experts measured the mean pixel value on the region of interest (ROI) of three cross-sectional images at different hepatic levels (green); 2. AI-3D: AI-measured mean voxel value on the volumetric automatic segmentation (blue); 3. AI-2D: AI-measured mean pixel value on a single axial slice containing the largest cross-sectional area among segmentations (blue); 4. AI-ROI: AI-measured mean pixel value on regions of interest (blue) at three different hepatic levels. Three slices were chosen, including one slice with the largest cross-sectional area and two neighborhood slices 5 mm away from the center slice. One center slice with ROI was shown as an example. NLST = National Lung Screening Trial.

### Study Design and Datasets

This retrospective study aims to generalize findings of a deep learning system that was developed to predict the existence of hepatic steatosis via plain chest CTs (Fig. 1). This study was conducted in accordance with the Declaration of Helsinki guidelines and received approval from the local institutional review board. A waiver of consent was obtained from the institutional review board as the analyzed data came from public datasets or conducting a retrospective study.

To evaluate the generalizability of this deep learning system, 1,014 CT images were collected from 8 publicly available, de-identified patient datasets. Each set of images was downloaded and curated from the following databases (Fig. 2): LIDC-IDRI<sup>21</sup>, NSCLC-Lung1<sup>22</sup>, RIDER<sup>23</sup>, VESSEL12<sup>24</sup>, MIDRC-RICORD-1A<sup>25</sup>, MIDRC-RICORD-1B<sup>25</sup>, COVID-19-Italy<sup>26</sup>, and COVID-19-China<sup>27</sup>. Four datasets<sup>25–27</sup> were initially obtained to diagnose COVID-19, three datasets<sup>21–23</sup> were scanned for lung cancer detection, and one dataset<sup>24</sup> was released for lung vessel segmentation. Non-contrast enhanced chest CT image was the only data inclusion criterion. The following image modalities were thus excluded: (i) contrast-enhanced chest CT images, which were selected out by an automatic method<sup>28</sup> and then validated by a radiologist; (ii) stomach with contrast agent; (iii) imaged liver with severe artifacts; livers with tumors or cysts collectively bigger than 5 cm<sup>3</sup>. Fig. 2 summarizes the amount of CT images in each validation dataset. A more detailed description of each dataset can be seen in the supplements.

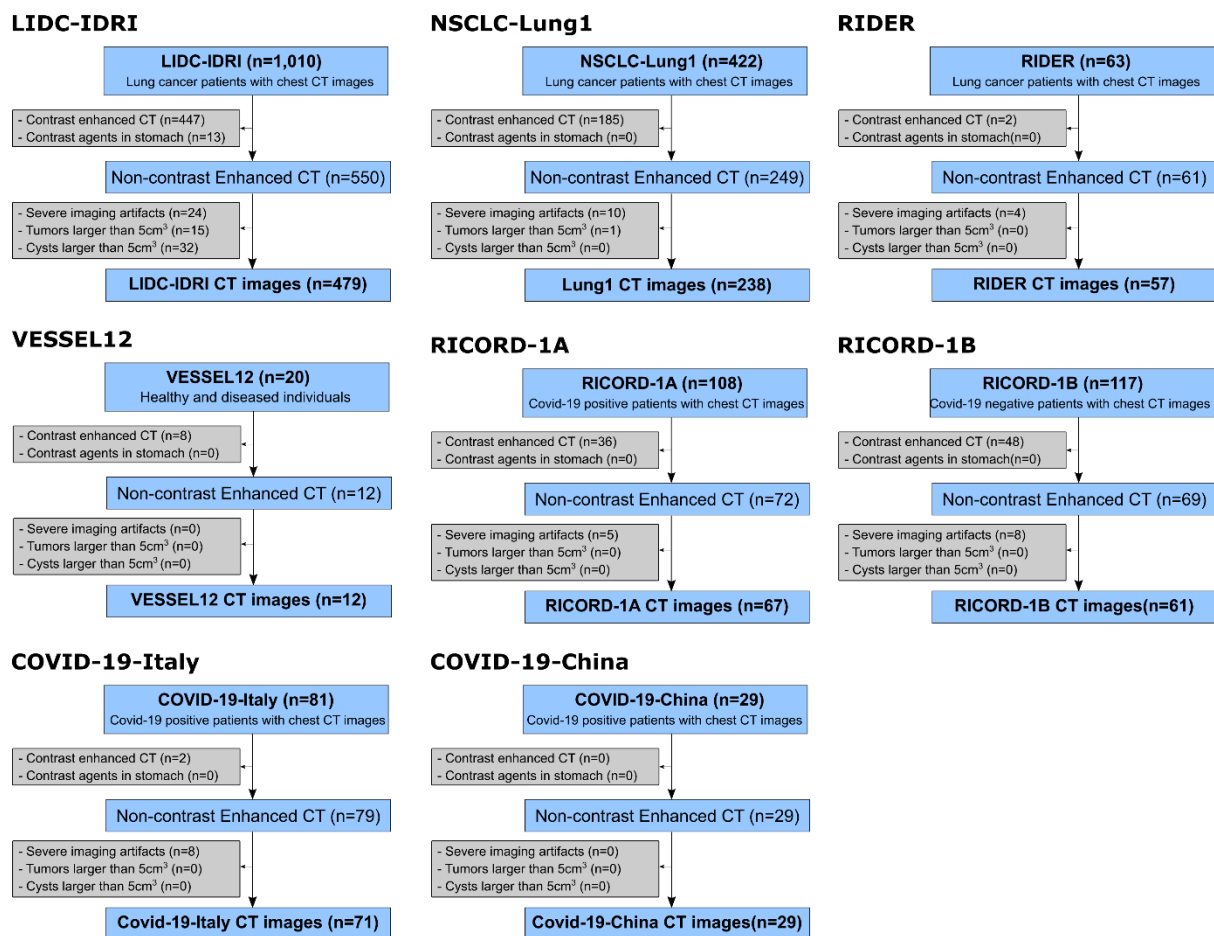


**Figure 2:** Consort diagram for each test dataset.

## **Data preprocessing**

CT images were reformatted to the Neuroimaging Informatics Technology Initiative (NIfTI) format. Linear interpolations were used to resample CT images to a common voxel spacing of 0.7 x 0.7 x 2.5 mm/pixel. CT Hounsfield units were windowed to [-200, 250] and rescaled to [0,1]. No data augmentation techniques were adopted during training or external validations.

## **Expert Annotated Liver Segmentation and Steatosis Classification**

Imaged livers were manually segmented and classified regarding the steatosis condition. Manual segmentations were conducted independently by seven trained individuals and then validated/corrected by a radiologist (Y.H., 10 years of experience). Reader experiences varied from 1 data scientist and 6 medical doctors (1, 10, 10, 10, 10, and 15 years of experience). Liver contour lines were drawn by readers on axial plain CT images of 2.5-mm thickness, from which the volumetric liver segmentations were automatically constructed by the 3D Slicer software (Version 5).

Liver fat content was estimated by liver attenuation and was measured on three separate 2D slices by selecting three circular regions with an area of around 2 cm<sup>2</sup>. Non-parenchymal regions were placed to avoid heterogeneity such as hepatic veins, bile ducts, and focal nodules. ROI attenuations were measured to capture the full spectrum of liver fat. Manual measures were performed without knowing the automated steatosis category. Reader experience varied from 1 data scientist, 6 medical doctors (1, 10, 10, 10, 10, 15 years of experience) to 1 radiologist (Y.H., 10 years of experience). Hepatic steatosis was annotated as positive by experts if the liver attenuation  $\leq 40$  HU.

## **Deep Learning Algorithm for Liver Segmentation and Hepatic Steatosis Classification**

We validate a deep learning system that is able to automatically detect hepatic steatosis from a given CT scan. The system consists of three consecutive steps: (1) liver segmentation, (2) liver fat quantification, and (3) hepatic steatosis classification. This deep learning system is fully automatic and end-to-end. In the liver segmentation, a modified 3D U-Net was implemented without retraining. 3D U-Net<sup>29</sup>, adopting an encoder-decoder architecture with skip connections, was initially purposed for biomedical image segmentation. We used a 3D U-Net model that was modified with residual connections and developed for liver segmentations on asymptomatic heavy smokers screening for lung cancer<sup>20</sup>. The modified 3D U-Net model architecture is shown in Fig. S1. In the model output, the largest connected component was retained by the connected-component

analysis and designated as the liver. All marked liver voxels were compared to the expert to derive the segmentation accuracy.

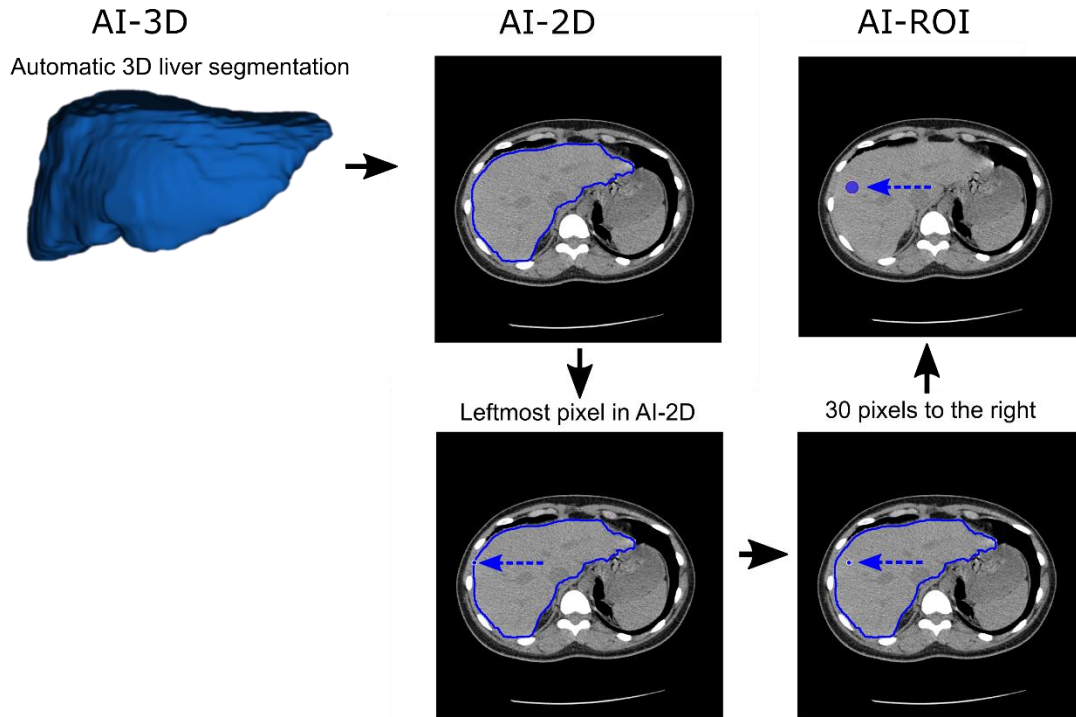


**Figure 3:** Liver attenuation was measured by artificial intelligence (AI) in three different ways. **AI-3D:** AI-calculated mean voxel value on the volumetric automatic segmentation; **AI-2D:** AI-calculated mean pixel value on a single axial slice which has the biggest cross-sectional segmentation area; **AI-ROI:** AI-calculated the mean pixel value on regions of interests of three cross-sectional slices at different hepatic levels (blue). Three slices were chosen as the AI-2D slice and two neighborhood slices with a distance of 5 mm. One center slice was shown here as an example.

Livers are labeled positive for hepatic steatosis if the automated measurements of liver attenuation are  $\leq 40$  HU. In our study, liver attenuation is measured via deep learning in three ways: AI-3D, AI-2D, and AI-ROI (Fig. 3). AI-3D attenuation denotes attenuation derived from the three-dimensional voxel value of the automated segmentation. All voxels recognized as the liver were computed to get an AI-3D attenuation. AI-2D attenuation denotes attenuation derived from the two-dimensional pixel value of the sliced automated segmentation. All pixels recognized as liver in one axial slice were computed to get an AI-2D attenuation. The axial segmentation which has the biggest segmentation area was sliced to represent the 3D segmentation. AI-ROI attenuation denotes attenuation by calculating the mean pixel value on three regions of interest (ROI) placed automatically by the AI. Three slices were chosen as one slice with the biggest cross-sectional segmentation area plus two



neighborhood slices with a distance of 5 mm. The center of circular ROI was set by 30-pixel-right to the leftmost pixel in each sliced segmentation. This optimized 30-pixel distance was derived empirically from our experience to ensure the ROI placed within the liver. The radius of the circular ROI was set at around 10 pixels to make up an area of around 2.0 cm<sup>2</sup>. A random group (n=87) was chosen from the LIDC-IDRI dataset to test agreements of attenuation by multiple experts and AI methods.

## **Statistical Analysis**

AI-generated segmentations were compared to expert segmentations using the Dice coefficient, Jaccard coefficient, Hausdorff distance, and average symmetric surface distance with standard deviations (Python package: medpy.metric.binary, Version 0.4.0). In liver attenuation measurements, two-sided Kolmogorov-Smirnov tests (Python package scipy.stats, Version 1.5.3) were conducted to test if attenuations follow a normal distribution and if AI and expert measurements follow the same distribution. Spearman's correlation coefficient (Python package scipy.stats, Version 1.5.3) and intraclass coefficient (Statistical software SPSS version 25, two-way random absolute agreement, single measures) were calculated for the correlation between manual and automatic measurements. In steatosis categorization, the area under the curve (AUC), sensitivity, and specificity from receiver operating characteristics (ROC) were rated for the AI performance (Python package: sklearn.metrics, Version 0.23.2) and bootstrap sampling (n=1000) was used to derive the 95% confidence interval (CI) of categorization performances.

## **RESULTS**

### **Dataset Characteristics**

A total of 1,014 chest CT images were used to validate the three-step AI system for hepatic steatosis detection (Fig. 1): (i) 3D liver segmentation; (ii) liver attenuation measurements; (iii) hepatic steatosis classification. A total of 786 (77.5%) CT images were scanned for lung cancer and 228 (22.5%) for COVID-19 prospectively. 931 (91.8%) were normal liver and 83 (8.2%) were hepatic steatosis annotated by experts. Table S1 summarizes the characteristics of each dataset.

### **AI Performance on 3D Liver Segmentation**



The automatic segmentations were compared to expert segmentations and achieved a DSC of  $0.957 \pm 0.046$  (mean  $\pm$  std). Box plots show DSC distributions of each validation set on which the normal and steatosis condition was compared (Fig. 4). There is a clear trend toward better segmentation accuracy on normal livers: DSC is  $0.959 \pm 0.040$  on normal livers but  $0.925 \pm 0.081$  on the liver with steatosis. Examples of automatic segmentations in comparison to the manual are shown in Fig. 4. Separate performances of each validation set in DSC, Jaccard Coefficient, Hausdorff distance, and average symmetric surface distance are shown in Table S1.

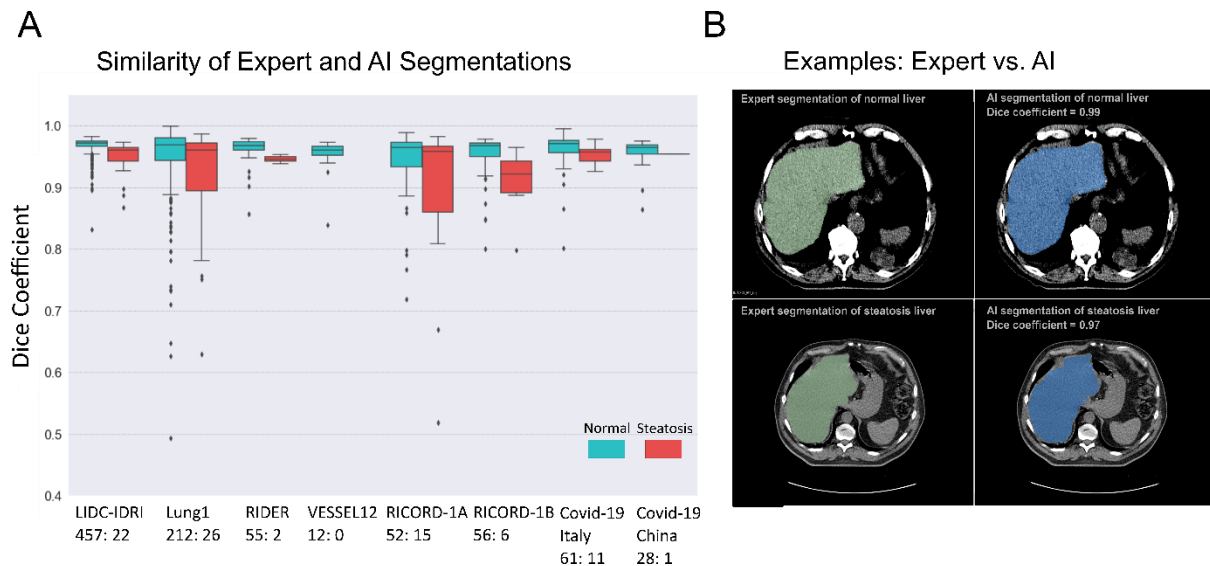


**Figure 4. A:** DSC between the deep learning system (AI) and expert segmentations grouped by expert annotations of normal and steatosis. **B:** Each example image was sliced from the CT scan with the AI (blue) and expert (green) segmentations. DSC = Dice coefficient.

### AI Performance on Liver Attenuation Measurement and Steatosis Classification

We compared the AI measurements to expert measurements to evaluate the automated liver fat quantification method and the subsequent steatosis classification. All measurements of AI and experts do not follow normal distributions. In the attenuation comparison, with the smallest MSE (2.355) and differences in mean (-0.464), AI-ROI is not significantly different from the expert measurements ( $P = 0.545$ ). Both AI-3D and AI-2D yielded significantly different results from the expert ( $P < 0.0001$ ), as shown in Fig. 5. A. Examples of the automatic attenuation measurements in comparison to ROI placed by experts are shown in Fig. 5. B. Intraclass coefficient (ICC) is shown in Table 1 as the comparison of measurements between AI methods and experts.

In the steatosis classification, AUC, sensitivity, and specificity were shown in Table 1 as well, along with the 95% confidence interval. Though AI-ROI attenuation measurements were not

significant, it is the AI-3D that achieved the best classification performance in all metrics. Scatter plots of attenuation comparison and confusion matrix can be seen in Fig. S2&S3.

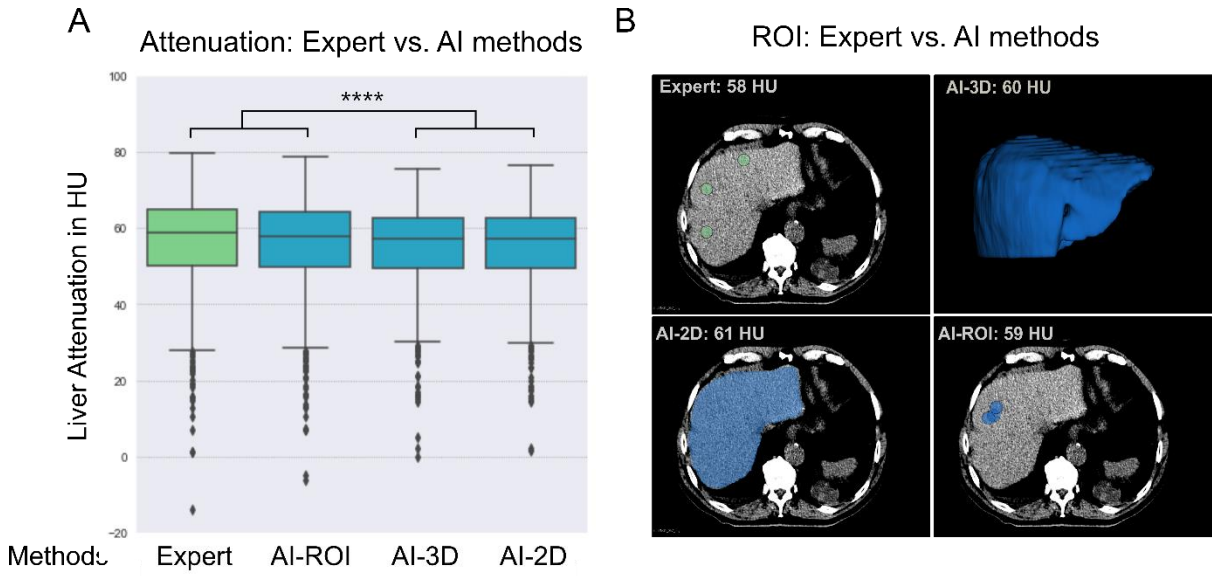


**Figure 5. A:** Box plots show liver attenuation measured by experts (green) and three automatic (blue) methods. Correlations are not labeled if differences are not significant. \*\*\*,  $p < 0.001$ ; \*\*,  $p < 0.01$ ; \*,  $p < 0.05$ . Spearman correlation and AUC are shown at the bottom. **B:** Examples of the quantification methods by expert and AI methods on the same CT image. Quantification of the liver attenuation was shown in the head of each image. Three ROIs were placed in three different hepatic levels but were shown in one image here for a vivid visualization.

Measurement	Mean $\pm$ Std	ICC (95% CI)	AUC (95% CI)	Sensitivity (95% CI)	Specificity (95% CI)
Expert	56.33 $\pm$ 11.69	-	-	-	-
AI-ROI	55.86 $\pm$ 11.92	0.963 (0.957 - 0.967)	0.921 (0.883 - 0.959)	0.855 (0.779 - 0.929)	0.987 (0.980 - 0.994)
AI-3D	54.94 $\pm$ 10.35	0.961 (0.927 - 0.976)	0.939 (0.903 - 0.973)	0.880 (0.807 - 0.948)	0.999 (0.997 - 1.000)
AI-2D	55.11 $\pm$ 10.27	0.952 (0.930 - 0.966)	0.894 (0.850 - 0.938)	0.795 (0.709 - 0.882)	0.994 (0.988 - 0.998)

**Table 1:** Performances of AI methods in liver attenuation measurements and hepatic steatosis classification. ICC = Intraclass coefficient; 95% CI = 95% confidence interval; AUC = the area under curve.

### Liver Attenuation Concordance among Experts vs. AI Measurements

The live attenuation was independently measured by four human experts and three artificial intelligence (AI) methods. All measurements of AI and human experts do not follow the normal distribution. AI-ROI measurements are not significantly different from all four experts. AI-3D and AI-2D are not significantly different for the two experts (N.Z. & Z.W.) but not for the other two experts (Z.Z. & F.X.). The statistical differences between experts and AI

methods can be seen in Fig. 6. A. ROI placement examples of the AI-ROI and experts are shown in Fig. 6. B.

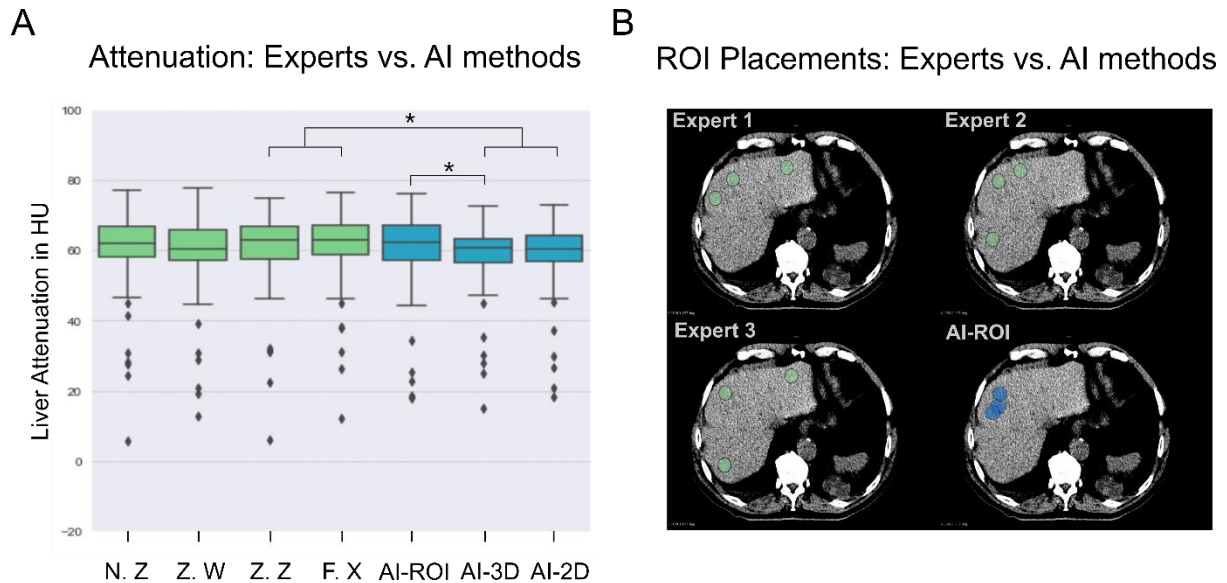


**Figure 6. A:** Liver attenuation between four human experts and automatic measurements in 87 CT scans randomly selected from the LIDC-IDRI validation set. N. Z., Z. W., Z. Z., and F. X. are four human experts, and AI denoted the automatic measurement. Correlations are not labeled if differences are not significant. \*\*\*,  $p < 0.001$ ; \*\*,  $p < 0.01$ ; \*,  $p < 0.05$ . **B.** One CT was measured by three human experts (green) and AI-ROI (blue). Three regions were placed in three different hepatic levels but were shown in one image here for a vivid visualization.

## Discussion

In this study, we externally validated a fully automatic deep learning system for hepatic steatosis detection on non-enhanced chest CT scans. This system demonstrated generalizable robust performance without needing prior retraining for the 3D liver segmentation, liver fat quantification, and steatosis classification. The deep learning system allowed fast and reliable detections of hepatic steatosis in millions of CT images that were scanned to determine other medical conditions, including lung cancer and COVID-19 diseases. The remarkable prediction accuracy is thus unbiased since CT was scanned without concerns of fatty liver beforehand. In other words, the low pre-test probability of the external datasets even strengthened the generalizability. With high generalizability, this method could help clinicians worldwide to detect early-stage hepatic steatosis as the first externally validated deep-learning method. This validation could enhance the current non-invasive hepatic steatosis diagnostics.

We chose to validate this deep learning system<sup>20</sup> because it firstly applied deep learning to liver segmentations on non-contrast enhanced chest CT scans. Other automatic methods either did not use deep learning<sup>17,18</sup> or did not use plain chest CT scans<sup>19,30</sup>. Overall, Deep-learning segmentations demonstrated high accuracies with our efforts to include large-scale external validation datasets; despite the slight decrease in accuracy from internal<sup>20</sup> to our external validations (mean DSC 0.970 vs 0.957), the external accuracy remains high. The difference in accuracy might be attributed to different CT imaging parameters. We also observed that the segmentation accuracy in the steatosis group is mostly lower than in the normal liver. One reason might be that the deep learning model was trained mostly on normal livers of CT images and therefore biased. The other reason might be the different textures and brightness in CT images. Retraining the model with more livers with steatosis might correct the biased segmentations.

Through our deep-learning method, the AI-ROI approach in liver fat quantification best mimic that of an expert. Region placements and measurements by AI-ROI are both not significantly different from those of experts. With an AUC is 0.921 (1 means perfect), we believe AI-ROI classification performance is comparable to human expert performance. We attribute the imperfection to the inter-reader variability within the ROI methodology since this near-perfect AUC of 0.921 was only compared to the CT reads from one single expert. Thus, the AUC of AI-ROI may be higher or lower, depending heavily on the opinions of an individual. To address this concern, we further proved that AI-ROI did not favor one particular expert by demonstrating no significant differences compared to four human experts. This is of great importance, as the validated deep learning system would help to reduce labor-intensive manual work and inter-reader variability in liver attenuation measurements.

Liver attenuation was also automatically measured by AI-3D and AI-2D in our study and the measurements are statistically significantly different from that of experts'. The reason might be that AI-3D and AI-2D segmentations include non-parenchymal regions, while the ROI method samples a parenchymal portion. However, AI-3D achieves a higher AUC, sensitivity, and specificity than AI-ROI in hepatic steatosis classification. The reason might be that AI-3D derives the volumetric attenuation therefore not subject to sampling errors. Future studies are recommended to prove the superiority and prognostic value of the volumetric attenuation.

The current non-invasive, standard clinical imaging methods to quantify liver fat quantification includes ultrasound, MRI, and CT images<sup>31</sup>. In this study, we focus on non-enhanced chest CT images for two reasons: CT's high statistical correlation with hepatic

steatosis<sup>6,7</sup> and for the abundance of data, as millions of people already underwent CT scans for lung cancer<sup>10,11,32</sup> and COVID-19<sup>12,33</sup>. While CT scans are continually ordered, CT's utility in detecting hepatic steatosis remains unexplored.

Our study contains four innovations that are immensely beneficial to clinical practice and AI algorithm developments: (i) the automated method is explainable: liver segmentation and the subsequent classification of hepatic steatosis are clearly visualized on CT images; (ii) this deep-learning method was externally validated on eight distinct datasets, thus demonstrating generalizability across CT imaging protocols of different clinical centers as well as potential patient demographical differences, accounting for any potential regional, national, and racial differences. This generalizability would effectively minimize the concern of AI biases for clinical application. (iii), this method can boost clinical efficiency, as the AI requires mere seconds to quantify liver fat, allowing clinicians to be able to review evidence of steatosis in a timely manner. (iv), the expert segmentations contained herein are to be released to the public freely to promote deep-learning segmentation algorithms. Since deep learning requires large datasets to fulfill its potential, publicly available datasets have already promoted deep-learning algorithms on contrast-enhanced CT images by only 200 liver segmentations<sup>30</sup> or 300 kidney segmentations<sup>34</sup>. We believe that our released 1,014 liver segmentations would advance greatly the deep learning algorithm on non-enhanced chest CT images.

Despite the innovative aspects, limitations of this study still exist. For instance, hepatic steatosis could be also defined by a liver-to-spleen attenuation ratio of less than 1, in addition to the metric used in this study (liver attenuation of less than 40 HU); however, only the latter definition was used in this AI system. Further optimized AI systems may need to include the liver-to-spleen ratio. Another limitation of our method lies in the intrinsic limitations to our dataset: this AI system was validated using chest CT scans. The inferior lobes of the liver may be incomplete in our dataset, potentially contributing to biased predictions. Another source of bias comes from the underlying patient population who, despite not necessarily being diagnosed with hepatic steatosis at presentation, are still mostly unhealthy due to lung cancer or COVID-19. To ensure the generalizability of this screening method, more validation datasets containing mostly healthy volunteers are necessary. Some other limitations of this AI system include its lack of prognostic value, as participant demographics and their underlying disease progression were not available. Furthermore, the manual segmentations could be biased, since only 1 of the 7 physicians who participated was a radiologist. Having a cohort of experts in radiology may provide more convincing ground truths.

In conclusion, we externally validated a fully automated segmentation-based method for hepatic steatosis detection across CT imaging protocols and clinical centers, as well as participants' regions, nations, and races. It allows a fast and reliable quantification of hepatic steatosis at chest CTs on lung cancer and COVID-19 datasets. With explainability and generalizability, the deep learning system can detect and therefore prevent early-stage hepatic steatosis from progressing to end-stage liver failures in international populations.

### **Data Availability**

Our study materials are collected and reformatted from publicly available datasets under their copyright licenses (Table S1). The reformatted CT images and 3D manual segmentations can be seen in Google Drive [https://drive.google.com/drive/folders/1-g\\_zJeAaZXYXGqL1OeF6pUjr6KB0igJX](https://drive.google.com/drive/folders/1-g_zJeAaZXYXGqL1OeF6pUjr6KB0igJX) or Baidu Wangpan <https://pan.baidu.com/s/1nRv-FJU4HtQ4nXi9H9145Q?pwd=2022> (passcode: 2022).

### **Code availability**

The deep-learning method is adopted from this study<sup>20</sup> and therefore not available here.

### **Acknowledgments**

The authors thank the support of Dr. Hugo Aerts for accessing the automatic method. This study was supported by a Fostering Foundation of the Second Hospital of Shandong University (Grant No. 2022YP46) and a Hainan Provincial Natural Science Foundation of China (Grant No. 821QN406).

### **Author Contributions**

X.L. and Y.H. equally contributed to this project. Detailed author contributions are as follows: Figures: Z.Z.; Code implementation and execution: Z.Z.; Code reviewing: Z.Y.; CT segmentation and annotation: All authors; Study design: Z.Z., Y.H., X.L.; Test data collection: Z.Z.; Data analysis and interpretation: Z.Z., Z.Y., J.L., Y.H.; Critical revision of the manuscript for important intellectual content: All authors; Statistical Analysis: Z.Z., Y.H., X.L.; Study supervision: Y.H., X.L.

### **References**

1. Nassir, F., Rector, R. S., Hammoud, G. M. & Ibdah, J. A. Pathogenesis and Prevention of Hepatic Steatosis. *Gastroenterol. Hepatol.* **11**, 167–175 (2015).

2. Palomar-Lever, A. *et al.* Hepatic steatosis as an independent risk factor for severe disease in patients with COVID-19: A computed tomography study. *JGH Open* **4**, 1102–1107 (2020).
3. Dam-Larsen, S. *et al.* Long term prognosis of fatty liver: risk of chronic liver disease and death. *Gut* **53**, 750–755 (2004).
4. Targher, G., Tilg, H. & Byrne, C. D. Non-alcoholic fatty liver disease: a multisystem disease requiring a multidisciplinary and holistic approach. *Lancet Gastroenterol Hepatol* **6**, 578–588 (2021).
5. Bravo, A. A., Sheth, S. G. & Chopra, S. Liver biopsy. *N. Engl. J. Med.* **344**, 495–500 (2001).
6. Limanond, P. *et al.* Macrovesicular hepatic steatosis in living related liver donors: correlation between CT and histologic findings. *Radiology* **230**, 276–280 (2004).
7. Park, S. H. *et al.* Macrovesicular hepatic steatosis in living liver donors: use of CT for quantitative and qualitative assessment. *Radiology* **239**, 105–112 (2006).
8. Speliotes, E. K. *et al.* Liver fat is reproducibly measured using computed tomography in the Framingham Heart Study. *J. Gastroenterol. Hepatol.* **23**, 894–899 (2008).
9. Boyce, C. J. *et al.* Hepatic steatosis (fatty liver disease) in asymptomatic adults identified by unenhanced low-dose CT. *AJR Am. J. Roentgenol.* **194**, 623–628 (2010).
10. Zhou Q. *et al.* China National Lung Cancer Screening Guideline with low-dose computed tomography (2018 version). *Zhongguo Fei Ai Za Zhi* **21**, 67–75 (2018).
11. National Lung Screening Trial Research Team *et al.* The National Lung Screening Trial: overview and study design. *Radiology* **258**, 243–253 (2011).
12. Fang, Y. *et al.* Sensitivity of Chest CT for COVID-19: Comparison to RT-PCR. *Radiology* **296**, E115–E117 (2020).
13. Machnicki, S. *et al.* The Usefulness of Chest CT Imaging in Patients With Suspected or Diagnosed COVID-19: A Review of Literature. *Chest* **160**, 652–670 (2021).
14. Wang, L. *et al.* Trends in the application of deep learning networks in medical image analysis: Evolution between 2012 and 2020. *Eur. J. Radiol.* **146**, 110069 (2022).



15. Zeleznik, R. *et al.* Deep convolutional neural networks to predict cardiovascular risk from computed tomography. *Nat. Commun.* **12**, 715 (2021).
16. Zeleznik, R., Weiss, J., Taron, J. & Guthier, C. Deep-learning system to improve the quality and efficiency of volumetric heart segmentation for breast cancer. *NPJ digital* (2021).
17. Jirapatnakul, A. *et al.* Automated measurement of liver attenuation to identify moderate-to-severe hepatic steatosis from chest CT scans. *Eur. J. Radiol.* **122**, 108723 (2020).
18. Kullberg, J. *et al.* Automated analysis of liver fat, muscle and adipose tissue distribution from CT suitable for large-scale studies. *Sci. Rep.* **7**, 10425 (2017).
19. Graffy, P. M., Sandfort, V., Summers, R. M. & Pickhardt, P. J. Automated Liver Fat Quantification at Nonenhanced Abdominal CT for Population-based Steatosis Assessment. *Radiology* **293**, 334–342 (2019).
20. Zhang, Z. *et al.* Deep Learning-based Assessment of Hepatic Steatosis on chest CT. *arXiv [q-bio.QM]* (2022).
21. Armato, S. G., 3rd *et al.* The Lung Image Database Consortium (LIDC) and Image Database Resource Initiative (IDRI): a completed reference database of lung nodules on CT scans. *Med. Phys.* **38**, 915–931 (2011).
22. Aerts, H., Velazquez, E. R. & Leijenaar, R. T. H. Decoding tumour phenotype by noninvasive imaging using a quantitative radiomics approach. *Nature* (2014).
23. Zhao, B. *et al.* Evaluating variability in tumor measurements from same-day repeat CT scans of patients with non-small cell lung cancer. *Radiology* **252**, 263–272 (2009).
24. Rudyanto, R. D. *et al.* Comparing algorithms for automated vessel segmentation in computed tomography scans of the lung: the VESSEL12 study. *Med. Image Anal.* **18**, 1217–1232 (2014).
25. Tsai, E. B. *et al.* The RSNA International COVID-19 Open Radiology Database (RICORD). *Radiology* **299**, E204–E213 (2021).
26. Zaffino, P. *et al.* An Open-Source COVID-19 CT Dataset with Automatic Lung Tissue Classification for Radiomics. *Bioengineering (Basel)* **8**, (2021).

27. Kassin, M. T. *et al.* Generalized chest CT and lab curves throughout the course of COVID-19. *Sci. Rep.* **11**, 6940 (2021).
28. Ye, Z. *et al.* Deep learning-based detection of intravenous contrast enhancement on CT scans. *Radiol Artif Intell* **4**, e210285 (2022).
29. Çiçek, Ö., Abdulkadir, A., Lienkamp, S. S., Brox, T. & Ronneberger, O. 3D U-Net: Learning Dense Volumetric Segmentation from Sparse Annotation. in *Medical Image Computing and Computer-Assisted Intervention – MICCAI 2016* 424–432 (Springer International Publishing, 2016). doi:10.1007/978-3-319-46723-8\_49.
30. Bilic, P. *et al.* The Liver Tumor Segmentation Benchmark (LiTS). *arXiv [cs.CV]* (2019).
31. Starekova, J., Hernando, D., Pickhardt, P. J. & Reeder, S. B. Quantification of Liver Fat Content with CT and MRI: State of the Art. *Radiology* **301**, 250–262 (2021).
32. Yang, D., Liu, Y., Bai, C., Wang, X. & Powell, C. A. Epidemiology of lung cancer and lung cancer screening programs in China and the United States. *Cancer Lett.* **468**, 82–87 (2020).
33. Li, K. *et al.* The Clinical and Chest CT Features Associated With Severe and Critical COVID-19 Pneumonia. *Invest. Radiol.* **55**, 327–331 (2020).
34. Heller, N. *et al.* The state of the art in kidney and kidney tumor segmentation in contrast-enhanced CT imaging: Results of the KiTS19 challenge. *Med. Image Anal.* **67**, 101821 (2021).
35. Zaffino, P. COVID-19. *ImagEngLab* [https://www.imagenglab.com/newsite/covid-19/?eeListID=1&eeFolder=Single\\_patients](https://www.imagenglab.com/newsite/covid-19/?eeListID=1&eeFolder=Single_patients) (2020).

## SUPPLEMENTARY INFORMATION

### Supplementary Materials and Methods

**LIDC-IDRI:** The Image Database Resource Initiative (IDRI) was created to further advance the Lung Image Database Consortium (LIDC) in 2004<sup>21</sup>. The LIDC-IDRI contains a total of 1018 chest CT scans from 1010 patients, including both contrast-enhanced and non-enhanced CT scans. Images were collected from seven participating academic institutions and eight medical imaging companies in the USA. LIDC consists of diagnostic and lung cancer screening chest CT scans with annotated lung lesions. It is originally used to develop automated lung cancer detection and diagnosis. LIDC images were constructed from 4 scanner manufacturers and 17 different CT imaging models. The tube peak potential energies used for scan acquisition ranged from 120 to 140 kV. Tube current ranged from 40 to 627 mA. Slice thicknesses ranged from 0.6 to 4.0 mm. The reconstruction interval ranged from 0.45 to 5.0 mm. The in-plane pixel size ranged from 0.461 to 0.977 mm. Each CT scan was initially presented at a standard brightness/contrast setting without magnification. No participant demographics (age, gender, etc.) or clinical information is available for this dataset.

**NSCLC-Lung1:** NSCLC stands for non-small cell lung cancer. The Lung1 data set was released in 2014 which consisted of 422 NSCLC patients in the Netherlands<sup>22</sup>. 132 are women and 290 are men. The mean age was 67.5 years (range: 33–91 years). Patients were included if they have confirmed diagnoses of lung cancer or underwent treatment with curative intent. This dataset was initially proposed to assess the prognostic value of radiomic features for lung cancer. CT scans and clinical data were available in this study<sup>22</sup>.

**RIDER:** The RIDER data set consists of 31 patients with two CT scans acquired approximately 15 min apart<sup>23</sup>. Patients with non-small cell lung cancer were recruited in 2007. The mean age is 62.1 years (range, 29-82 years), 16 were men (mean age, 61.8 years; range, 29-79 years) and 16 were women (mean age, 62.4 years; range, 45-82 years). Parameters for the 16-detector row scanner were as follows: tube voltage, 120 kVp; tube current, 299-441 mA; detector configuration. Parameters of the 64-detector row scanner were as follows: tube voltage, 120 kV; tube current, 298-351 mA.

**VESSEL12:** This dataset is collected from the VESsel SEgmentation in the Lung (VESSEL12) challenge held in 2012<sup>24</sup>, which is to compare automatic methods of lung vessel segmentations taken from both healthy and diseased populations. CT scans were

collected from three hospitals in the Netherlands and Spain in a variety of clinically common scanners and protocols<sup>24</sup>. The dataset released 20 CT scans and around 10 scans contain abnormalities such as emphysema, nodules, or pulmonary embolisms.

**MIDRC-RICORD-1A & 1B:** Medical Imaging Data Resource Center (MIDRC); RSNA International COVID-19 Open Radiology Database (RICORD); Release-1A: Chest CT COVID Positive (MIDRC-RICORD-1a); Release-1B: Chest CT COVID Positive (MIDRC-RICORD-1b)<sup>25</sup>. The data was collected in April 2020. Each dataset consists of 120 chest CT scans from four international sites: the USA, Turkey, Canada, and Brazil. The dataset has two inclusion criteria: 1. Adults underwent chest CT scans for suspected COVID-19 infection; 2. COVID-19 positive (1A) confirmed by one or more conditions: reverse-transcription polymerase chain reaction test, immunoglobulin M antibody test, or clinical diagnosis using hospital-specific criteria.

**COVID-19-Italy:** The dataset is originally made of 62 COVID-19-positive patients and then enriched to 81 patients<sup>26,35</sup>. The group of 62 patients underwent non-contrast chest CT scans in Italy in 2020. The average age was 56 years (range 20–83), and the male/female ratio was 23/27. Images were obtained with two different scanners with reconstructions of the volume at 0.3 to 1 mm slice thickness. Automatic lung tissue classification, clinical score, and intensive care unit information are provided as well. We chose the enriched set with one CT scan per patient, therefore adding up to 81 CT images in our study.

**COVID-19-China:** The dataset is made of 29 COVID-19-positive Chinese patients who received multiple non-contrast chest CTs between January 21st and April 12th, 2020 in Hubei Province, China<sup>27</sup>. The patients were predominantly female (69%, 20/29), and were  $41 \pm 10$  years old (range 25 to 60 years old). Each patient underwent multiple CT scans at different time points. We chose the baseline CT scans per patient and therefore added up to 29 CT images in our study.

## Supplementary Tables

Dataset	Initial Purpose	License	Location
LIDC-IDRI	Lung cancer	CC BY 3.0	USA
NSCLC-Lung1	Lung cancer	CC BY 3.0	Netherlands
RIDER	Lung cancer	CC BY 3.0	USA
VESSEL12	Lung vessel segmentation	Not specified at source	Netherlands, Spain
RICORD-1A	COVID-19 positive	CC BY-NC 4.0	USA, Canada, Turkey, Brazil
RICORD-1b	COVID-19 negative	CC BY-NC 4.0	USA, Canada, Turkey, Brazil
COVID-19-Italy	COVID-19 positive	CC BY-NC 4.0	Italy
COVID-19-China	COVID-19 positive	CC BY 4.0	China

**Table S1:** The amounts of images of interest were denoted for each dataset. Four datasets were initially obtained to diagnose COVID-19, three datasets were scanned for lung cancer detection, and one dataset was released for lung vessel segmentation. These CT images were scanned from eight countries and released by copyright licenses. CC-BY refers to the Creative Commons Attribution license and allows readers to distribute, remix, adapt, and build upon the material in any medium or format, so long as attribution is given to the creator. NC means for noncommercial purposes only.

Dataset	Dice Coefficient	Jaccard Coefficient	Hausdorff Distance	ASSD
LIDC-IDRI	0.967 ± 0.015	0.937 ± 0.027	21.391 ± 27.202 mm	0.932 ± 1.434 mm
Lung1	0.942 ± 0.070	0.898 ± 0.107	28.605 ± 43.447 mm	1.611 ± 3.660 mm
RIDER	0.962 ± 0.020	0.927 ± 0.036	19.817 ± 12.230 mm	0.970 ± 0.793 mm
VESSEL12	0.948 ± 0.035	0.903 ± 0.059	59.155 ± 85.549 mm	3.668 ± 5.868 mm
RICORD-1A	0.930 ± 0.083	0.879 ± 0.123	26.472 ± 16.907 mm	1.626 ± 1.883 mm
RICORD-1B	0.948 ± 0.041	0.903 ± 0.068	21.144 ± 14.934 mm	0.903 ± 0.068 mm
COVID-19-Italy	0.957 ± 0.023	0.925 ± 0.048	27.754 ± 20.072 mm	1.222 ± 0.980 mm
COVID-19-China	0.960 ± 0.028	0.918 ± 0.040	18.668 ± 8.694 mm	0.917 ± 0.420 mm
<b>Total</b>	<b>0.957 ± 0.046</b>	<b>0.920 ± 0.071</b>	<b>24.131 ± 31.253 mm</b>	<b>1.210 ± 2.255 mm</b>

**Table S2:** AI Liver segmentation performances on each dataset separately and conclusively. ASSD = average symmetric surface distance.

## Supplementary Figures

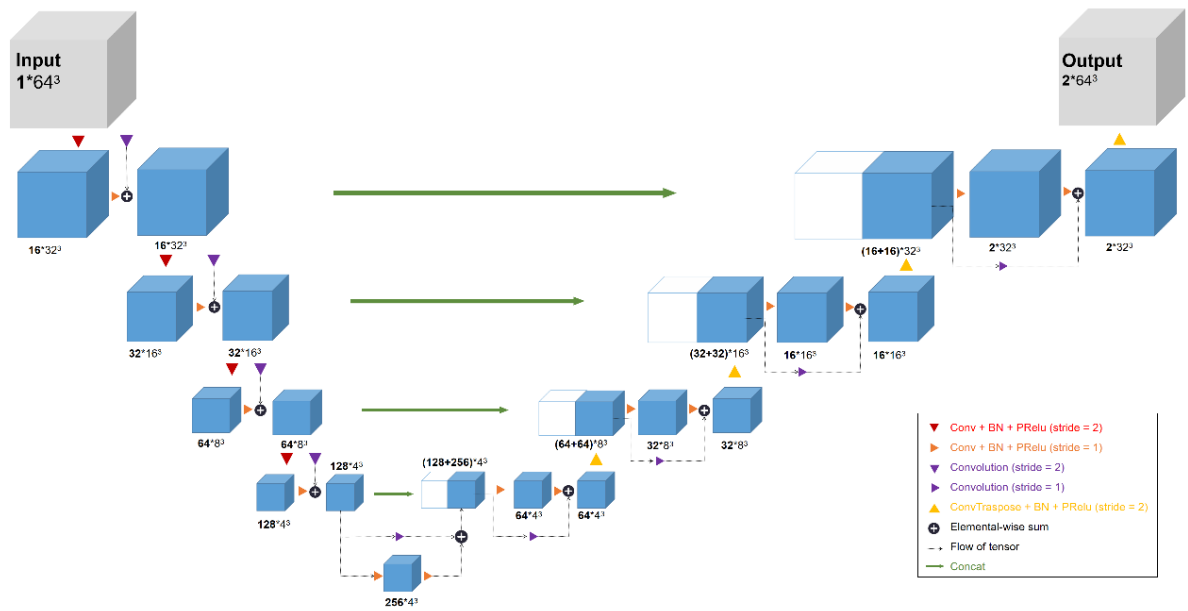


**Figure S1:** The model architecture of the 3D U-Net for volumetric liver segmentation. Prelu= parametric rectified linear unit, BN = batch normalization.

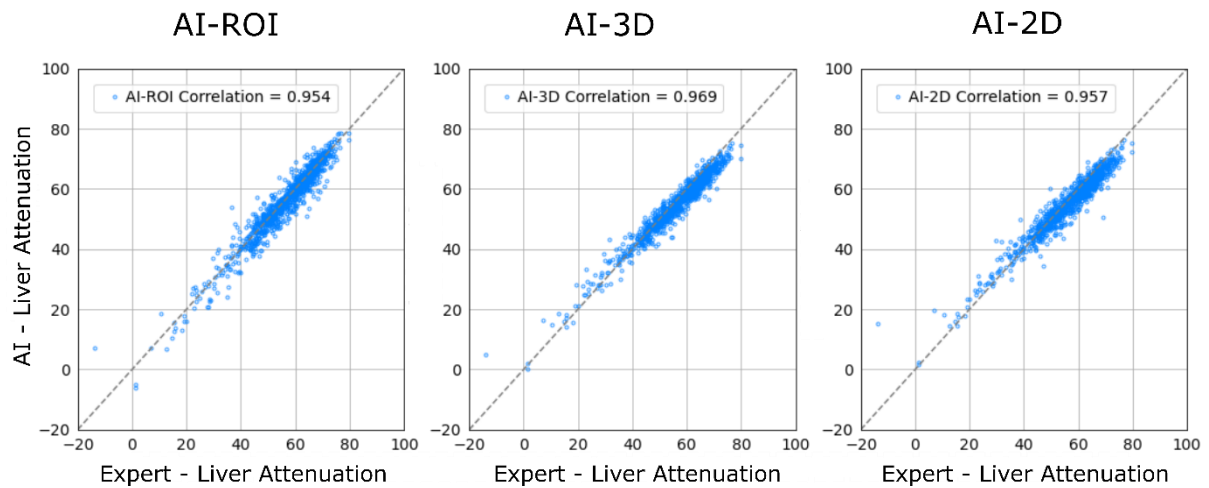


**Figure S2:** Scatter plots show liver attenuation measured in HU by AI methods and expert readers. The Spearman correlation is denoted.

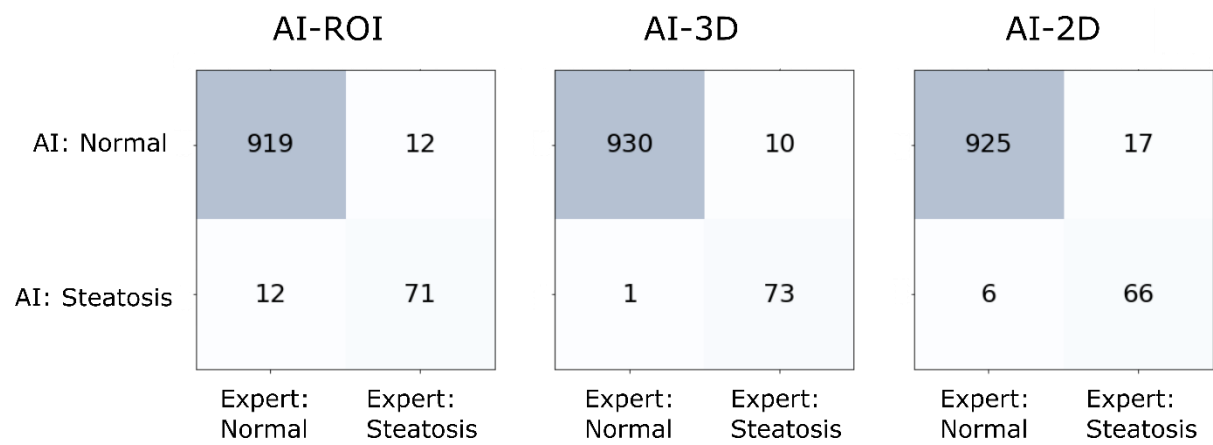


**Figure 3:** Confusion matrices were conducted to compare the steatosis categorization by AI methods and expert readers.